Defense Technical Information Center
Compilation Part Notice

ADP013625

TITLE: Numerical Simulation of Complex Flow Around a 85 degree Delta Wing

DISTRIBUTION: Approved for public release, distribution unlimited

This paper is part of the following report:

TITLE: DNS/LES Progress and Challenges. Proceedings of the Third AFOSR International Conference on DNS/LES

To order the complete compilation report, use: ADA412801

The component part is provided here to allow users access to individually authored sections of proceedings, annals, symposia, etc. However, the component should be considered within the context of the overall compilation report and not as a stand-alone technical report.

The following component part numbers comprise the compilation report:
ADP013620 thru ADP013707

NUMERICAL SIMULATION OF COMPLEX FLOW AROUND A 85° DELTA WING

H. SHAN, L. JIANG, C. LIU

Department of Mathematics
University of Texas at Arlington, Arlington, Texas, U.S.A.

Abstract.

The three-dimensional separated flow around a slender flat-plate delta wing with sharp leading-edge at a 12.5° angle of attack has been studied by solving the full compressible Navier-Stokes equations in the generalized curvilinear coordinates. The time integration is carried out by using the second-order LU-SGS implicit scheme. A fourth-order centered compact difference scheme is used for spatial derivatives. A sixth-order implicit filter is employed to reduce numerical oscillation. Non-reflecting boundary conditions are imposed at the far-field and outlet boundaries to avoid possible non-physical wave reflection. Parallel computing based on Message Passing Interface (MPI) has been utilized to improve the performance of the code.

Two Reynolds numbers have been selected. At a lower Reynolds number of 5×10^4 based on the chord length and the freestream velocity, the flow is stable and dominated by a pair of leading-edge primary vortices. At a higher Reynolds number of 1.96×10^5, the small-scale vortex shedding is observed near the leading-edge of the delta wing. The computational results are compared with the experimental work of Riley & Lowson (1998). The periodic shedding of small-scale vortical structures near the leading-edge has been studied in detail, and the vortex shedding is found to be associated with the Kelvin-Helmholtz-type instability and the secondary vortex. The period of vortex shedding is obtained from the time series of the three velocity components recorded near the leading-edge. The time-averaged features of the vortical structures are also discussed.

1. Introduction

Recent developments in aerospace technology have revived the interest to the study of flow separations around an aircraft maneuvering dynamic operations. Understanding of the complex separated vortical flow is crucial to the aerodynamic design of modern aircraft. Vortical structures, which develop over the leading-edge extension, slender fore-body, and main wing, may have severe effect on the aerodynamic characteristics and performance of modern fighter aircraft.

A flat-plate delta wing with sharp leading-edge provides a simple configuration to investigate the development of the vortical structures. The experimental study of delta wing started in the early 1950's. The experimental results have shown that the flow over the suction side of a delta wing at a high angle of attack is dominated by a pair of counter-rotating vortices, i.e. the leading-edge primary vortices. These vortices are formed as a result of the rolling-up of the vortex sheet shedding from the leading-edge. The flow induced by the leading-edge vortices separates near the wing surface and forms a pair of oppositely rotating secondary vortices. At large sweep angle, the size and strength of the leading-edge vortices increase with the angle of incidence, resulting in a substantial nonlinear lift increment, sometimes called vortical lift. But the maximum lift of a delta wing is limited by a phenomenon known as vortex breakdown(Visser & Nelson 1993).

The breakdown of the primary vortex has drawn considerable attentions. Payne *et al.* (1988) used smoke flow visualization and laser sheet technique to study the vortical flow field above the delta wing at high angles of attack. Two types of vortex breakdown were testified, i.e. the bubble mode and the spiral mode. However, as it was pointed by Rieley & Lowson (1998), most studies have been concentrated on the nature and breakdown of the primary vortex instead of the leading-edge shear layer itself. Actually, there are several mechanisms associated with the leading-edge shear layer. The most obvious one is the Kelvin-Helmholtz instability of two-dimensional free shear layer. Two types of instabilities are observed in experiments, i.e. the unsteady, and steady instability. The experimental study carried out by Gad-el-Hak and Blackwelder (1985) using dye visualization has shown the unsteady instability, where small-scale vortices are shed from the leading-edge, travel up and around the shear layer, and finally feed into the core of large-scale leading-edge vortex. The pairing of the small-scale vortices were observed in the same experiment. The experiential observation of the pairing of Kelvin-Helmholtz type vortex during flow separation around a delta wing was confirmed by Lowson (1988). Similar phenomenon has been reported in a simple tow-dimensional shear layer (Winant & Browand, 1974). It is generally found that the phenomena as-

sociated with the traveling Kelvin-Helmholtz instability in strongly curved shear layer are parallel to the effects observed in a two-dimensional free shear layer. The experiments also indicate that the unsteady instability is exceptionally sensitive to external disturbance. The steady instability was observed in the experiment of Payne et $al.$ (1988). The static small-scale vortical-like structures were found in the shear layer of a delta wing with a 85° sweep angle and at 40° angle of attack. The growth of these structures was found to be similar to the evolution of the classic Kelvin-Helmholtz instability. In this experiment, the pairing of the small-scale vortices was not observed. The stationary cellular substructures that do not rotate around the primary vortex were also observed by Honkan & Andreopoulos (1997) in their experiment. The recent experimental work of Rieley & Lowson (1998) revealed, using flow visualization and laser Doppler anemometer measurement, the existence of static small vortical structures in the free shear layer shedding from the sharp leading-edge of a delta wing. A local three-dimensional Kelvin-Helmholtz-type instability was suggested by the authors for the formation of these vortical structures in the free shear layer. Similar vortical structures were also observed in the investigations of Cipolla & Rockwell (1998), where small-scale concentrations of vorticity form near the leading-edge of a rolling delta wing. These vortices appear to evolve in a coupled fashion, which has been considered as the wake-like instability.

Numerical simulations of vortex breakdown above a stationary sharp edged delta wing over a range of angles of attack were carried out by Modiano & Murman (1994). Their computation was based on an Euler solver with adaptive mesh system. The spiral form of vortex breakdown was observed without the emergence of the small-scale vortical structures inside the shear layer. In the numerical investigation by Argwal et $al.$ (1992), the well-known Euler/Navier-Stokes code CFL3D was used to simulate the leading-edge vortex breakdown of a low-speed flow on a flat-plate delta wing with sharp leading-edges. Although the vortex breakdown positions obtained from the computation were reported in good agreement with experimental data, the small-scale vortices were not observed, which could be attributed to the lack of numerical resolution/accuracy. A numerical investigation of the unsteady vortex structure over a 76° sweep wing at 20.5° angle of attack was carried out by Gordnier & Visbal (1994). Their numerical calculation indicated that the small-scale vortical structures emanated from the leading-edge was brought on by the Kelvin-Helmholtz-type instability. Pairing of the small vortices was not observed in the computational results. No computational result has indicated the existence of the steady instability.

The intend of present work is to study the mechanism of the shear layer

instability of a slender flat-plate delta wing with sharp leading-edges at a fixed angle of attack. High-resolution numerical simulation is employed to give a detailed description of flow instability and vortex shedding near the leading-edge of the delta wing. The interactions between the small-scale vortical structures and the primary vortex is also studied.

2. Governing Equations

The three-dimensional compressible Navier-Stokes equations in generalized curvilinear coordinates (ξ, η, ζ) are written in conservative forms:

$$\frac{1}{J}\frac{\partial Q}{\partial t} + \frac{\partial(E - E_v)}{\partial \xi} + \frac{\partial(F - F_v)}{\partial \eta} + \frac{\partial(G - G_v)}{\partial \zeta} = 0 \qquad (1)$$

The flux vectors are

$$Q = \begin{pmatrix} \rho \\ \rho u \\ \rho v \\ \rho w \\ e \end{pmatrix} \quad E = \frac{1}{J}\begin{pmatrix} \rho U \\ \rho U u + p\xi_x \\ \rho U v + p\xi_y \\ \rho U w + p\xi_z \\ U(e+p) \end{pmatrix} \quad F = \frac{1}{J}\begin{pmatrix} \rho V \\ \rho V u + p\eta_x \\ \rho V v + p\eta_y \\ \rho V w + p\eta_z \\ V(e+p) \end{pmatrix}$$

$$G = \frac{1}{J}\begin{pmatrix} \rho W \\ \rho W u + p\zeta_x \\ \rho W v + p\zeta_y \\ \rho W w + p\zeta_z \\ W(e+p) \end{pmatrix} \qquad E_v = \frac{1}{J}\begin{pmatrix} 0 \\ \tau_{xx}\xi_x + \tau_{yx}\xi_y + \tau_{zx}\xi_z \\ \tau_{xy}\xi_x + \tau_{yy}\xi_y + \tau_{zy}\xi_z \\ \tau_{xz}\xi_x + \tau_{yz}\xi_y + \tau_{zz}\xi_z \\ q_x\xi_x + q_y\xi_y + q_z\xi_z \end{pmatrix}$$

$$F_v = \frac{1}{J}\begin{pmatrix} 0 \\ \tau_{xx}\eta_x + \tau_{yx}\eta_y + \tau_{zx}\eta_z \\ \tau_{xy}\eta_x + \tau_{yy}\eta_y + \tau_{zy}\eta_z \\ \tau_{xz}\eta_x + \tau_{yz}\eta_y + \tau_{zz}\eta_z \\ q_x\eta_x + q_y\eta_y + q_z\eta_z \end{pmatrix} \qquad G_v = \frac{1}{J}\begin{pmatrix} 0 \\ \tau_{xx}\zeta_x + \tau_{yx}\zeta_y + \tau_{zx}\zeta_z \\ \tau_{xy}\zeta_x + \tau_{yy}\zeta_y + \tau_{zy}\zeta_z \\ \tau_{xz}\zeta_x + \tau_{yz}\zeta_y + \tau_{zz}\zeta_z \\ q_x\zeta_x + q_y\zeta_y + q_z\zeta_z \end{pmatrix}$$

where J is Jacobian of the coordinate transformation, and $\xi_x, \xi_y, \xi_z, \eta_x, \eta_y, \eta_z, \zeta_x,$ ζ_y, ζ_z are coordinate transformation metrics. τ_{kl}'s and q_k's are the viscous stress and the heat flux, respectively.

In Eq. (1), a second order Euler Backward scheme is used for time derivatives, and the fully implicit form of the discretized equations is given by

$$\frac{3Q^{n+1} - 4Q^n + Q^{n-1}}{2J\Delta t} + \frac{\partial(E^{n+1} - E_v^{n+1})}{\partial \xi}$$
$$+ \frac{\partial(F^{n+1} - F_v^{n+1})}{\partial \eta} + \frac{\partial(G^{n+1} - G_v^{n+1})}{\partial \zeta} = 0$$

$$(2)$$

Q^{n+1} is estimated iteratively as:

$$Q^{n+1} = Q^p + \delta Q^p \tag{3}$$

where,

$$\delta Q^p = Q^{p+1} - Q^p \tag{4}$$

At step $p = 0$, $Q^p = Q^n$; as δQ^p is driven to zero, Q^p approaches Q^{n+1}. The flux vectors are linearized as follows:

$$
\begin{aligned}
E^{n+1} &\approx E^p + A^p \delta Q^p \\
F^{n+1} &\approx F^p + B^p \delta Q^p \\
G^{n+1} &\approx G^p + C^p \delta Q^p
\end{aligned}
\tag{5}
$$

So that Eq. (2) can be written as:

$$[\frac{3}{2}I + \Delta t J(D_\xi A + D_\eta B + D_\zeta C)]\delta Q^p = R \tag{6}$$

where R is the residual:

$$R = -(\frac{3}{2}Q^p - 2Q^n + \frac{1}{2}Q^{n-1}) - \Delta t J[(D_\xi(E - E_v) + D_\eta(F - F_v) + D_\zeta(G - G_v)]^p \tag{7}$$

D_ξ, D_η, D_ζ represent partial differential operators, and A, B, C are the Jacobian matrices of flux vectors:

$$A = \frac{\partial E}{\partial Q}, \qquad B = \frac{\partial F}{\partial Q}, \qquad C = \frac{\partial G}{\partial Q} \tag{8}$$

The right hand side of Eq. (6) is discretized using fourth-order compact scheme (Lele, 1992) for spatial derivatives, and the left hand side of the equation is discretized following LU-SGS method (Yoon & Kwak, 1992). In this method, the Jacobian matrices of flux vectors are split as:

$$A = A^+ + A^-, \quad B = B^+ + B^-, \quad C = C^+ + C^-$$

where,

$$A^\pm = \frac{1}{2}[A \pm r_A I], \quad B^\pm = \frac{1}{2}[B \pm r_B I], \quad C^\pm = \frac{1}{2}[C \pm r_C I] \tag{9}$$

and,

$$r_A = \kappa max[|\lambda(A)|] + \tilde{\nu}, \quad r_B = \kappa max[|\lambda(B)|] + \tilde{\nu}, \quad r_C = \kappa max[|\lambda(C)|] + \tilde{\nu}$$

where $\lambda(A), \lambda(B), \lambda(C)$ are eigenvalues of A, B, C respectively, κ is a constant greater than 1. $\tilde{\nu}$ is taken into account for the effects of viscous terms, and the following expression is used:

$$\tilde{\nu} = max[\frac{\mu}{(\gamma - 1)M_r^2 R_e P_r}, \frac{4}{3}\frac{\mu}{R_e}]$$

The first-order upwind finite difference scheme is used for the split flux terms in the left hand side of Eq. (6). This does not effect the accuracy of the scheme. As the left hand side is driven to zero, the discretization error will also be driven to zero. The finite difference representation of Eq. (6) can be written as:

$$[\frac{3}{2}I + \Delta t J(r_A + r_B + r_C)I]\delta Q_{i,j,k}^p = R_{i,j,k}^p$$
$$-\Delta t J \quad [\quad A^- \delta Q_{i+1,j,k}^p - A^+ \delta Q_{i-1,j,k}^p$$
$$+ \quad B^- \delta Q_{i,j+1,k}^p - B^+ \delta Q_{i,j-1,k}^p$$
$$+ \quad C^- \delta Q_{i,j,k+1}^p - C^+ \delta Q_{i,j,k-1}^p \quad] \tag{10}$$

In LU-SGS scheme, Eq. (10) is solved by three steps. First initialize δQ^0 using

$$\delta Q_{i,j,k}^0 = [\frac{3}{2}I + \Delta t J(r_A + r_B + r_C)I]^{-1}R_{i,j,k}^p$$

In the second step, the following relation is used:

$$\delta Q_{i,j,k}^* = \delta Q_{i,j,k}^0 + [\frac{3}{2}I + \Delta t J(r_A + r_B + r_C)I]^{-1}$$
$$\times [\Delta t J(A^+ \delta Q_{i-1,j,k}^* + B^+ \delta Q_{i,j-1,k}^* + C^+ \delta Q_{i,j,k-1}^*)]$$

For the last step, δQ^p is obtained by

$$\delta Q_{i,j,k}^p = \delta Q_{i,j,k}^* - [\frac{3}{2}I + \Delta t J(r_A + r_B + r_C)]^{-1}$$
$$\times [\Delta t J(A^- \delta Q_{i+1,j,k}^p + B^- \delta Q_{i,j+1,k}^p + C^- \delta Q_{i,j,k+1}^p)]$$

The sweeping of the computational domain is performed along the planes of $i + j + k = const$, i.e. in the second step, sweeping is from the low-left corner of the grid to the high-right corner, and then vice versa in the third step.

In order to depress numerical oscillation caused by central difference scheme, a spatial filtering is used instead of artificial dissipation. Implicit sixth-order compact scheme for space filtering (Lele, 1992) is applied for primitive variables u, v, w, ρ, p after each time step.

For subsonic flow, u, v, w, T are prescribed at the inflow boundary, ρ is obtained by solving modified N-S equation based on the characteristic analysis. On the far field and out flow boundary, non-reflecting boundary conditions are applied. Adiabatic, non-slipping conditions are used for the wall boundary. All equations of boundary conditions are solved implicitly with internal points. Specific details of boundary treatment can be found in Jiang *et al* (1999).

3. Computational Details

Numerical simulation has been implemented to investigate the compressible flow separation around a slender delta wing. The geometry of the delta wing, taken from the experimental work of Rieley & Lowson (1998), is shown in Figure 1. The sweep angle denoted by Λ is 85° and the leading-edge angle denoted by σ is 30°. The chord length is taken as the characteristic length L, such that the non-dimensional chord length is $c = 1.0L$. The non-dimensional thickness of the delta wing is $h = 0.024L$. The freestream velocity U_∞ is the characteristic velocity.
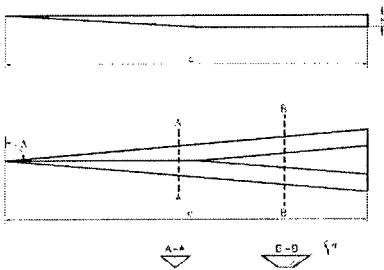

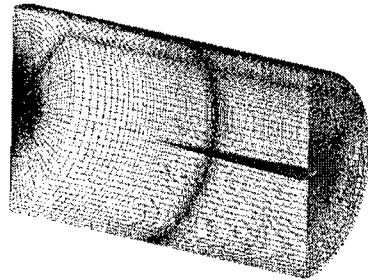*Figure 1*. Schematic of the delta wing

Figure 2.   H-C type grid around a 85° sweep delta wing

3.1. GRID GENERATION

An H-C type mesh system for a half-plane model of the delta wing is used based on the assumption that the flow is symmetrical to the the half-plane. The mesh is H-type in the meridian section and C-type in the cross section. An elliptic grid generation method, first proposed by Spekreijse (1995), is used to generate the three-dimensional grids. This method is based on a composite mapping, which is consisted of a nonlinear transfinite algebraic transformation and an elliptic transformation. The grids are orthogonal on the delta wing surface. The sharp leading-edge is approximated by a round

edge with a small radius of $1.0 \times 10^{-3} L$, while in the experiment of Rieley & Lowson (1998), the average thickness of the leading-edge was 0.12 mm, which was approximately $2.55 \times 10^{-4} L$. Computations are carried out on three meshes, i.e. one lower resolution mesh with $140 \times 70 \times 70$ grid nodes and two higher resolution meshes with $180 \times 150 \times 70$, and $180 \times 250 \times 120$ grid nodes, where the three numbers N_ξ, N_η, N_ζ in the sequence $N_\xi \times N_\eta \times N_\zeta$ are corresponding to grid numbers in ξ, η, and ζ directions of the computational domain. In the physical domain, the ξ, η, and ζ directions are approximately corresponding to the axial, azimuthal, and wall-normal directions, respectively. An example of the three-dimensional grid is displayed in Figure 2, where only the grids of inflow- and outflow boundaries, and the far field are displayed.

3.2. PARALLEL COMPUTING

The parallel version of the numerical simulation code based on the Message Passing Interface (MPI) has been developed to improve the performance. The parallel computing is combined with domain decomposition method. The computational domain is divided into n equal-sized subdomains along the ξ direction as shown in Figure 3, where n is the number of processors. This is a simple partition with a balanced load for each processor. During computation, a processor communicates with it neighbors through exchanging the data at left and right boundary of each subdomain. But this type of communication is not suitable for calculating derivative in the ξ direction while using the compact finite difference scheme. If each grid node along a ξ grid line locates in the same processor, it will be straightforward to use the compact scheme. In Figure 4, a data structure with four processors is used as an example to illustrate a special type of data exchange which has been utilized to accomplish the data structure transformation. The top figure shows the original partition where the computational domain is divided along the ξ direction. This data structure can be transformed to a new structure shown in the bottom figure where the domain is divided along the ζ direction. The transformation is accomplished by first defining two new data types and then calling a MPI routine "MPI_ALLTOALL" from the MPI library. In the new data structure, all the grid nodes along a ξ grid line are stored in one processor. After the calculation of derivative is completed, an inverse transformation is used to the transfer the data structure back to original partition.

A test case has been used to evaluate the performance of the MPI code to calculate the derivatives in the ξ, η, and ζ directions on a $480 \times 160 \times 80$ grid. The performance of a parallel computing is measured by the speedup $S(n,p)$ which is defined as the ratio of the runtime of a serial program to the
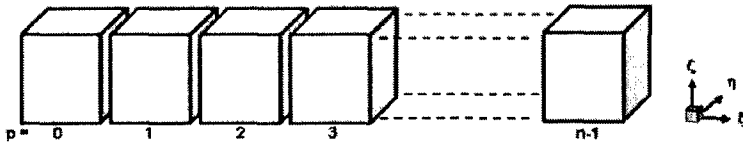
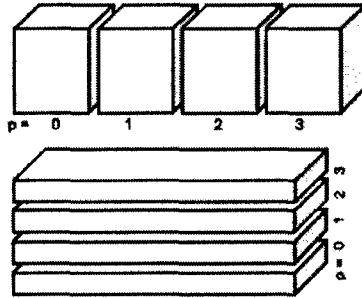*Figure 3.*   The domain decomposition along ξ direction in the computational space

Figure 4.   The change of data structure for calculating derivative in ξ direction using the compact scheme.

runtime of the parallel program. In Figure 5, the speedups on a SGI Origin 2000 computer are displayed as a function of the number of processors. The dashed line represents the linear speedup. Super-linear performance has been achieved to calculate derivatives in the η, and ζ directions where no data exchange is required. In the ξ direction, the speedup is much lower because of the massive data exchange in the data structure transformation introduced above.

Next, the total performance of the MPI code to simulate the flow around the delta wing has been tested and compared with the serial code compiled using the automatic parallelization option provided by SGI MIPSpro 7 Fortran 90 compiler. The comparison is displayed in Figure 6, where the performance of the parallel code running on 4, 6, and 15 processors is much better than the serial code. For the parallel simulation of flows around the delta wing, 10 processors have been used on a grid of $180 \times 150 \times 70$ and 12 processors have been used on a $180 \times 250 \times 120$ grid.

4. Results and Discussions

4.1. GENERAL FEATURES

All results presented here are obtained from numerical simulation of flow around a $85°$ sweep delta wing with a flat-plate suction surface, which has
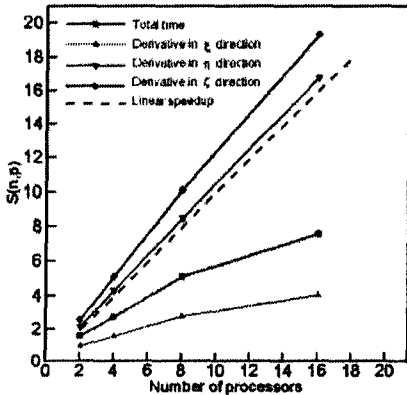
Figure 5. Speedup $S(n,p)$ of calcula-
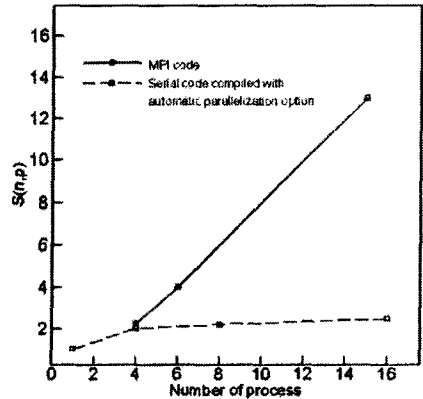tion of derivatives in ξ, η, and ζ direc-
tions.

Figure 6. Speedup $S(n,p)$ of parallel
computing using MPI compared with
using automatic parallelization

been introduced in Section 3. The angle of attack is fixed at $12.5°$. The
free-stream Mach number is $Ma = 0.1$.

The numerical simulation of three cases has been carried out. In case 1,
the Reynolds number based on the chord length and the free-stream velocity
is $Re_c = 5 \times 10^4$. The number of grid is $140 \times 70 \times 70$. In case 2 and 3, the
Reynolds number is $Re_c = 1.96 \times 10^5$. The grid numbers are $180 \times 150 \times 70$
for case 2 and $180 \times 250 \times 120$ for case 3. No initial or boundary disturbance
are imposed for all three cases. Therefore, the dependence of the instability
to the external disturbance has not been covered in the current work.

4.1.1. *Case 1*
The flow is stable at $Re_c = 5 \times 10^4$. The contours of the axial vorticity on
selected cross sections are displayed in Figure 7. It is quite clear that a pair
of counter-rotating vortices, so called the leading-edge primary vortices,
appears over the suction side of the delta wing. These vortices form as a
result of flow separation and the rolling-up of the vortex sheet shedding
from the leading-edge. The primary vortices are steady and stable at this
Reynolds number. The primary vortices are composed of a pair of counter-
rotating oblique vortex tubes starting from the apex of delta wing, from
a three-dimensional point of view. Beneath the primary vortices, near the
suction surface of the delta wing, the secondary vortices, which have an
opposite rotating direction to the primary vortices, are formed as a result
of the spanwise outflow induced by the primary vortex. Figure 8 shows
the iso-surface of the instantaneous axial vorticity above the suction sur-
face the delta wing. The computational results are in good agreement with
the experimental results of Riley & Lowson (1998). During the computa-

tion for the high Reynolds number case, the flow becomes unsteady and small-scale vortical structures keep shedding from the leading-edge. In the experiment of Riley & Lowson (1998), flow instability was observed when the Reynolds number was raised above $Re_c = 100,000$. In order to study the flow instability near the leading edge, the numerical simulations with higher resolutions and a higher Reynolds number have been conducted, the results are discussed in next sections.
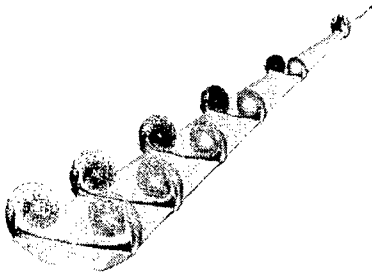

Figure 7.   Contours of the axial vorticity on selected cross sections, angle of attack $\alpha = 12.5°$, $Re = 5 \times 10^4$, $Ma = 0.1$
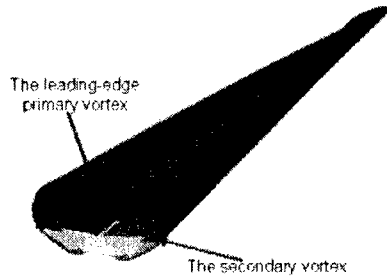
Figure 8.   Iso-surface of axial vorticity above the suction surface of a 85° sweep delta wing at an angle of attack $\alpha = 12.5°$, $Re = 5 \times 10^4$, $Ma = 0.1$

4.1.2. Case 2

At a higher Reynolds number, i.e. $Re_c = 1.96 \times 10^5$, flow instability occurs near the leading edge of the delta wing. In order to capture the small vortical structures observed in the experiment, the numerical simulation is accomplished on a $180 \times 150 \times 70$ grid which has a higher resolution. During the simulation, flow instability and periodic shedding of small vortical structures from the leading edge are observed. Since there is no disturbance imposed as the initial or boundary condition for the computation, the unstable behavior presented by the flow in the computational results are rather intrinsic.

The distributions of the instantaneous axial vorticity on various cross section are shown in Figure 9. Compared with the low Reynolds number results of Figure 7, the flow is still dominated by a pair of primary vortices. But instability appears at the leading-edge of delta wing, where vortex shedding is observed. On the suction surface near the leading-edge, the secondary vortices are still visible in this figure.

In Figure 10 the contours of axial vorticity at different time on a cross section at $x = 0.88L$ are displayed through (a) to (h), each frame is corresponding to a snapshot of a two-dimensional flow field at a certain time.
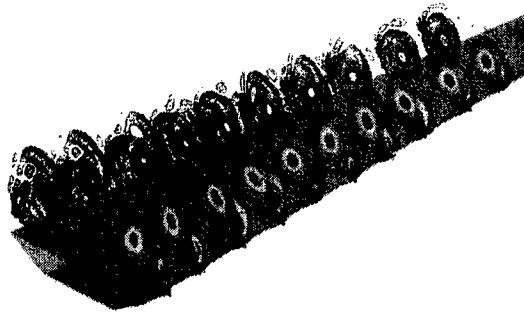
Figure 9. The instantaneous distributions of the axial vorticity on various cross sections. Angle of attack $\alpha = 12.5°$, $Re = 1.96 \times 10^5$, $Ma = 0.1$

Flow instability is quite obvious in these figures. The primary vortex deforms compared to the low Reynolds number case. The flow pattern inside the primary vortex resembles that of the spiral instability mode, which presented occasionally in the experiment of Rieley & Lowson(1998). Two strong shear layers are visible in Figure 10 through the concentration of axial vorticity contours. The first one is the leading-edge shear layer whose axial vorticity is positive (shown in light color in Figure 10), which wraps the leading-edge corner from below and feeds into the primary vortex. The other one lies between the primary vortex and the suction surface of the delta wing and has a negative axial vorticity (shown in dark color in Figure 10), which is associated with the secondary vortex. Therefore, the shear layer below the primary vortex is also called the secondary shear layer. As it will be discussed later, both the leading-edge shear layer and the secondary shear layers are related to the instability and vortex shedding process near the leading-edge.

Among the small-scale vortical structures shedding from the leading-edge, there are two types of vortices, distinguished by the direction of rotation or by the sign of axial vorticity. Those vortices whose rotating direction is the same as the primary vortex are named as the A-family vortices, which are corresponding to a positive axial vorticity component. The vortices rotating in the opposite direction as the primary vortex are called the B-family vortices and have a negative axial vorticity component. The A-family vortices are stronger than the B-family vortices, which can be recognized from the contours of the axial vorticity in Figure 10.

In Figure 10(a), a bulge is observed on the leading-edge shear layer. The bulge grows in size as it moves away from the leading edge, as shown in Figure 10(b), (c), and (d). This process is corresponding to the generation and shedding of the A-family vortex. Because the B-family vortices are very

weak, the shedding process of B-family vortices is not clear in Figure 10. However, in colored animations (not shown here), the pairing of the A-family and B-family vortices can be observed. A more detailed study reveals that the B-family vortex comes from the shedding of the secondary vortex.
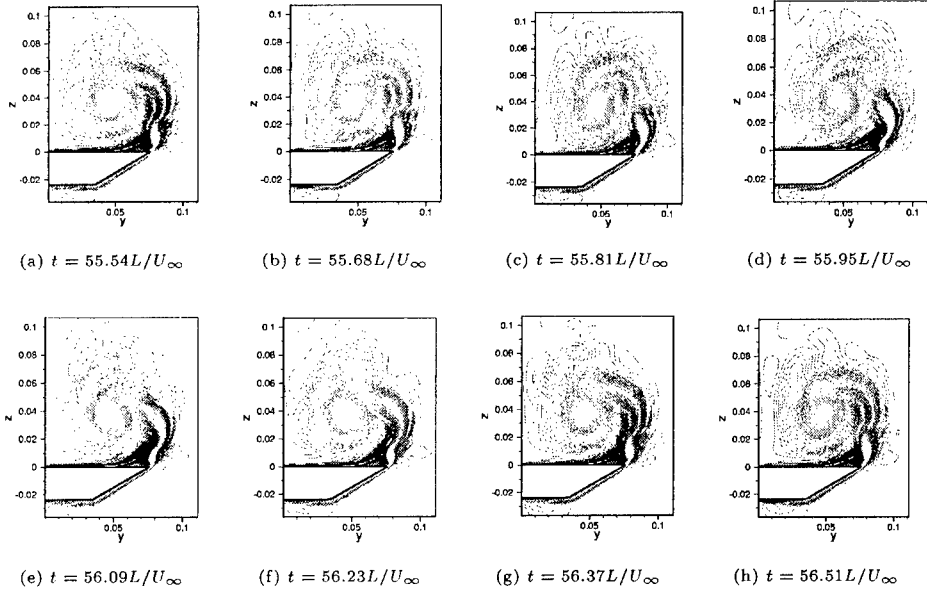

(a) $t = 55.54L/U_\infty$ (b) $t = 55.68L/U_\infty$ (c) $t = 55.81L/U_\infty$ (d) $t = 55.95L/U_\infty$

(e) $t = 56.09L/U_\infty$ (f) $t = 56.23L/U_\infty$ (g) $t = 56.37L/U_\infty$ (h) $t = 56.51L/U_\infty$

Figure 10. Contours of axial vorticity of different time on a cross section at $x = 0.88L$. Angle of attack $\alpha = 12.5°$, $Re = 1.96 \times 10^5$, $Ma = 0.1$

In Figure 10, frame (a) resembles frame (g). So frames (a) through (g) show one period of vortex shedding. The small-scale vortical structures shedding from the leading-edge are in turn captured by the primary vortex and feeding into the rolling-up process of the primary vortex. After leaving the leading-edge, both A- and B-family vortices experience severe deformation as they are stretched and captured by the primary vortex. The flow pattern inside the core of the primary vortex resembles that of the spiral instability mode, which is also observed in the experiment (Rieley & Lowson, 1998). In the numerical simulation, these small-scale vortical structures dissipate quickly as they are leaving the leading-edge and entering the central region of the primary vortex. But in the experiment the spiral instability can evolve into transition. The fast dissipation of the spiral mode in the numerical simulation can be attributed to the insufficiency of resolution. Because grids are clustered near the wall and near the leading-edge of delta wing, in the areas far away from the wall the resolution is relatively low. The stretching of the small-scale vortical structures is not depicted clearly, especially between the symmetrical plane and the core of the primary vortex.

As it is shown in Figure 10, the grid resolution in the areas far from the wall is not high enough. In the third case, the resolution has been increased in this area. The grid number is $180 \times 250 \times 120$. Because the Reynolds number is the same as the second case, the solution of case 2 has been interpolated to the mesh of case 3 and used as the initial field.

The contours of the instantaneous axial vorticity on selected cross-section are displayed in Figure 11. The cross-sectional view of the contours of instantaneous axial vorticity at $x = 0.88L$ is shown in Figure 12. Small-scale vortical structures are shedding from the leading edge. The pairing of small-scale vortices rotating in the opposite direction can also be recognized. Along the outer edge of the primary vortex, the structures are stretched as they are wrapped into the the vortex core. Compared with case 2, the higher resolution grid has clearly captured the small-scale structures as well as the phenomenon of vortex stretching. Although the stretched the vortical structures which can be considered as disturbance, are wrapped into the primary vortex, the flow in the core area is stable. No breakdown of the primary vortex has been observed in the computational result.
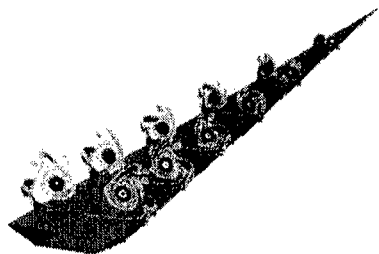

Figure 11. The instantaneous distributions of the axial vorticity on various cross sections. Angle of attack $\alpha = 12.5°$, $Re_c = 1.96 \times 10^5$, $Ma = 0.1$. The grid is $180 \times 250 \times 120$.
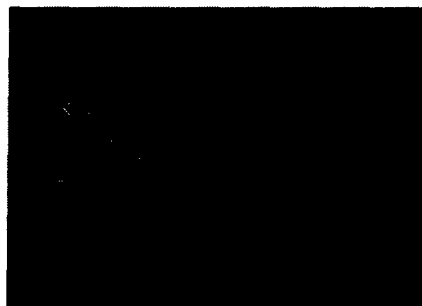
Figure 12. Cross-sectional view of the contours of instantaneous axial vorticity at $x = 0.88L$, Angle of attack $\alpha = 12.5°$, $Re_c = 1.96 \times 10^5$, $Ma = 0.1$. The grid is $180 \times 250 \times 120$.

In Figure 13, the limiting streamlines on the suction side of the delta wing are displayed. The attachment line along the symmetric line of the delta wing represents the attachment of the primary vortex. The position of the separation line indicates the location where the secondary vortex rolls up. The attachment line near the leading edge is cause by the attachment of the secondary vortex. The computational result agrees well with the schematic representations of the flow separation over a high swept delta wing (Delery, 2001). A spatial wandering of the separation line and the attachment line associated with the secondary vortex is also observed in the computational results.
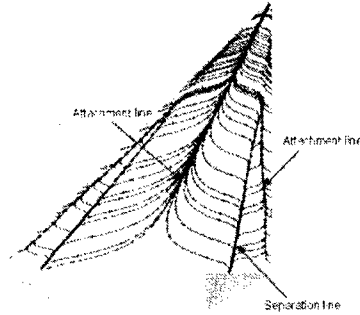
Figure 13. Instantaneous limiting streamline on the suction side of a delta wing. Angle of attack $\alpha = 12.5°$, $Re_c = 1.96 \times 10^5$, $Ma = 0.1$. The grid is $180 \times 250 \times 120$.

4.2. VORTEX SHEDDING NEAR THE LEADING-EDGE

Because the small-scale vortical structures are shedding continuously from the leading-edge, the area near the leading-edge is of particular interest in present work. The detailed pictures of vortex-shedding near the leading-edge is shown in Figure 14, where the projected streamline and contours of axial vorticity of various instance on a cross-section at $x = 0.88L$ are displayed. Through (a) to (h) in Figure 14, the pattern of projected stream-line exhibits a periodic feature. Actually, figures (a) to (g) fit in one period of variation. In Figure 14(a), there is a secondary vortex attaching on the suction surface of delta wing. The strong leading-edge shear layer is shown by dark color of the contours of axial vorticity. Near the leading-edge, the shear layer is concentrated in a narrow area. In Figure 14(b), at $t = 55.68L/U_\infty$, a small vortex shown by the projected streamline appears near the leading-edge over the free shear layer. In the same picture, a small bulge appears on the shear layer. The generation of this small vortex can be attributed to the Kelvin-Helmholtz instability. Therefore, the small vortex is named as the Kelvin-Helmholtz (K-H) type vortex. At the same time, the secondary vortex, which was attaching on the wing surface at $t = 55.54L/U_\infty$, moves away from the wall. As the K-H type vortex grows, the secondary vortex is pushed further away from the wall. From $t = 55.81L/U_\infty$ to $t = 55.95L/U_\infty$, (Figure 14(c) to (d)) the secondary vortex moves upward and begins to separate from the wall, which is corresponding to the B-family vortex, whose rotating direction is opposite to the primary vortex. Therefore, the B-family vortex comes from the shedding of the secondary vortex. The generation of the leading-edge K-H type vortex also causes the deformation of the shear layer, which is visible from the contours of the axial vorticity in Figure 14(b), (c), and (d). The bulge on the contours of axial vorticity is corresponding to the K-H type vortex.

In Figure 14(d), the secondary vortex almost disappears and the K-H type vortex is still attached to the leading-edge. In Figure 14(e) and (f), the K-H type vortex grows in size until it reaches the edge of the primary vortex. Another vortex appears at the same location of the secondary vortex, actually it is a new secondary vortex. The K-H type vortex gradually moves upward and sheds from the leading-edge, and comes out to be the A-family vortex, whose rotating direction is the same as the primary vortex. It is obviously that the A-family vortex originates from the K-H type leading-edge vortex. The last two frames are the periodic repeating of frames (a) and (b) in Figure 14.

The vortex-shedding near the leading-edge is a periodic process. The interaction between the secondary vortex and the leading-edge shear layer generates a K-H type vortex. As this K-H type vortex grows, the induced flow pushes the secondary vortex away form the wall, and ultimately leads to the shedding of the B-family vortex. The K-H type vortex grows in size as the secondary vortex shows up again near the wall. The induced flow pushes the K-H type vortex away form the wall and leads to the shedding of the A-family vortex. So the A-family vortex originates from the Kelvin-Helmholtz instability of shear flow near the leading-edge. The B-family vortex originates from the secondary vortex. The period of vortex shedding is between $0.89L/U_\infty$ and $0.98L/U_\infty$. The scale of the K-H type leading-edge vortex and the secondary vortex is about $0.005L$.

The interpretation of the above phenomena is based on the Kelvin-Helmholtz instability of cross-sectional two-dimensional flow. Considering many cross-sections simultaneously, the period of vortex shedding is the same, there is only phase difference between one cross-section and the other. From a three-dimensional point of view, the A- and B-family vortices become vortex tubes, which are oblique to the axial direction.

The time series of three components of the instantaneous velocity at a location near the leading-edge ($x = 0.88L$, $y = 0.076L$, $z = 0.0094L$) are recorded and shown in Figure 15, 16, and 17. This probe point locates on the cross-section shown in Figure 10 and Figure 14, so that the velocity signals can be interpreted in accordance with the two-dimensional vortex shedding pictures. The signals of the three components of velocity are all periodic functions of time. The axial velocity u has two local maximums and two local minimums within a period. There are only one local maximum and one local minimum within a period for the signals of the spanwise velocity v and the vertical velocity w. The phase difference between v and w is approximately $\pi/2$, which can be interpreted as a result of the small-scale vortical structure passing through the probe.

In order to compare the axial velocity signal with the vortex and shedding pictures in Figure 14, a part of Figure 15 has been enlarged and
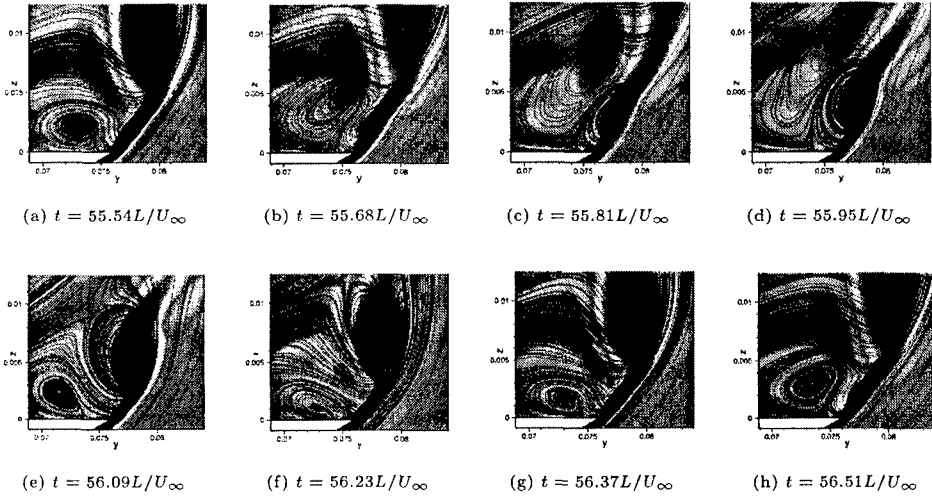
(a) $t = 55.54L/U_\infty$ (b) $t = 55.68L/U_\infty$ (c) $t = 55.81L/U_\infty$ (d) $t = 55.95L/U_\infty$

(e) $t = 56.09L/U_\infty$ (f) $t = 56.23L/U_\infty$ (g) $t = 56.37L/U_\infty$ (h) $t = 56.51L/U_\infty$

Figure 14.   Projected streamline and contours of axial vorticity of different time on a cross section at $x = 0.88L$. Angle of attack $\alpha = 12.5°$, $Re = 1.96 \times 10^5$, $Ma = 0.1$
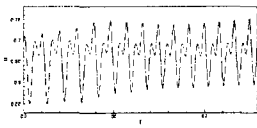

Figure 15. Instanta-neous axial velocity at a location of $x = 0.88L$, $y = 0.076L$, $z = 0.0094L$
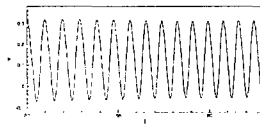
Figure 16. Instan-taneous spanwise veloc-ity at a location of $x = 0.88L$, $y = 0.076L$, $z = 0.0094L$
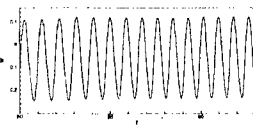
Figure 17. Instanta-neous vertical velocity at a location of $x = 0.88L$, $y = 0.076L$, $z = 0.0094L$

shown in Figure 18, where those points with the same time as the frames of Figure 14 have been marked with the same letter through (a) to (g). In Figure 18, one period starts at point (a) and ends at point (g). Compared with Figure 14, it has been found that the local minimum at point (d) with a smaller axial velocity value is corresponding to the B-family vortex. As the B-family vortex moves through the probe point, as shown in Fig-ure 14(c) and (d), the axial velocity u decreases from point (c) to point (d) and reaches its local minimum in Figure 18. Then the axial velocity recovers as the B-family vortex leaves the probe point. It is followed by the shedding of an A-family vortex from the leading-edge. Before the central part of the A-family vortex reaches the probe point, the axial velocity u signals recorded by the probe increases from point (e) to (f) in Figure 18. Then it decreases again from (f) to (g) as the core of the A-family vortex moves through the probe. Therefore, the local minimum at point (g) is as-sociated with the A-family vortex. The local minimum at point (g) has a

relatively larger value of axial velocity compared with the local minimum at point (d), which is related to the B-family vortex. The center of both A- and B-family vortices is low-momentum region. Since the B-family vortex originates from the shedding of the secondary vortex near the suction surface of the delta wing, and it brings fluid with lower axial velocity, the central part of the B-family vortex has a lower momentum. The A-family vortex comes from the shedding of leading-edge K-H type vortex. It brings fluid from the free shear layer, which has a relatively larger momentum. In Figure 18, the local maximum at point (b) is corresponding to frame (b) of Figure 14, where both the A- and B-family vortices have not separated from the delta wing. The signals of the spanwise and the vertical velocity can be interpreted in a similar way. In Figure 17, the local maximum is corresponding to the passing of a B-family vortex, where the vertical velocity is positive. The local minimum is corresponding to the passing of an A-family vortex, where the vertical velocity is negative. Thus the period of velocity signals reflects the elapsed time at which the A- and B-family vortices are shedding from the delta wing. Thus the period of vortex-shedding can be measured as the distance between the peaks of local maximums or local minimums on the signals of three velocity components.
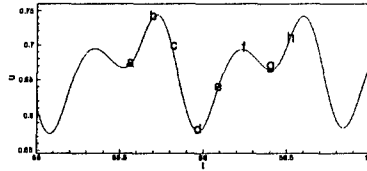

Figure 18. Instantaneous axial velocity at location $x = 0.88L$, $y = 0.076L$, $z = 0.0094L$

In order to estimate the vortex-shedding period more accurately, power spectrums of velocity fluctuations are calculated based on the velocity signals and shown in Figure 19, 20, and 21. The velocity fluctuation is calculated as the difference between the instantaneous velocity and the time-averaged mean velocity. There are two peaks in the spectrum of the axial velocity fluctuation shown in Figure 19. The frequency of the first peak is $1.086U_\infty/L$ and $2.31U_\infty/L$ for the second peak. There is only one peak in the spectrum of the spanwise and vertical velocity fluctuation. The peak frequency is $1.086U_\infty/L$, which is the same as the first peak of the u' spectrum in Figure 19. This peak frequency value $f = 1.086U_\infty/L$ represents the frequency of vortex shedding, the corresponding period is $T = 0.9208L/U_\infty$. The higher frequency in Figure 19, corresponding to a time period of $T = 0.433L/U_\infty$, reflects the elapsed time between the shedding of a A-family vortex and a B-family vortex, which is approximately half the period of the shedding of a single A- or B-family vortex.
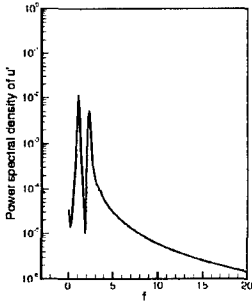
Figure 19. Power spec-
trum density of u' at
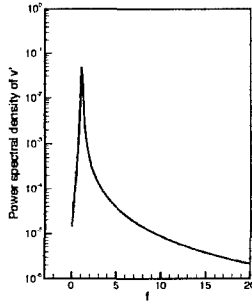location x = $0.88L$,
$y = 0.076L$, $z = 0.0094L$

Figure 20. Power spec-
trum density of v' at
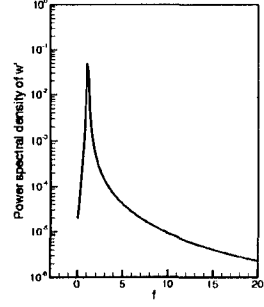location x = $0.88L$,
$y = 0.076L$, $z = 0.0094L$

Figure 21. Power spec-
trum density of w' at
location x = $0.88L$,
$y = 0.076L$, $z = 0.0094L$

4.3. TIME-AVERAGED RESULT

The time-averaged velocity profiles distributed on a spanwise line above
the suction surface of the delta wing on a cross section at $x = 0.88L$ is
shown in Figure 22. The distance between the spanwise line and the wing
surface is denoted by the vertical coordinate z in Figure 22. These results
are in good agreement with the experiments carried out by Rieley & Low-
son (1998). As it was stated by Rieley & Lowson (1998), the axial velocity
profile indicates the windward boundary layer separation. The inflection
point on the axial velocity profile is similar to the Kelvin-Helmholtz insta-
bility in plane mixing layers. In Figure 22(b), the spanwise velocity profile
near the surface (z=0.0002L) changes sign near $y = 0.0746L$, which is
corresponding to the re-attachment point of the secondary vortex. The in-
flection points on profiles of the vertical velocity component in Figure 22(c)
are corresponding to the edge of the leading-edge shear layer. The inflec-
tion point moves outboard as the distance from the wing surface increases.
The negative part of the vertical velocity is corresponding to the secondary
vortex. The secondary vortex is still visible in the time-averaged results.
The evidence of vortex shedding has been removed by the temporal aver-
age procedure. The point of inflection on the velocity profile is associated
with inviscid instability. Rayleigh's inflection point theorem, studying the
instability of a two-dimensional velocity profile based on the linear nor-
mal mode approach, points out that disturbance can be amplified at the
point of inflection. The physical interpretation of the theorem was given by
Lin (1945). The restoring mechanism will force a fluid particle displaced
vertically in either direction to return to its starting position. But at the
point of inflection the restoring mechanism is not present and disturbance
can grow. In the flow around the slender delta wing, the situation is more

complex. On the two-dimensional cross section plane, which is vertical to the axial direction, a strong shear layer is observed near the leading-edge, as shown in Figure 14(a). The existence of the secondary vortex increases the strength of the shear layer and provides more chance for the generation of the Kelvin-Helmholtz instability.
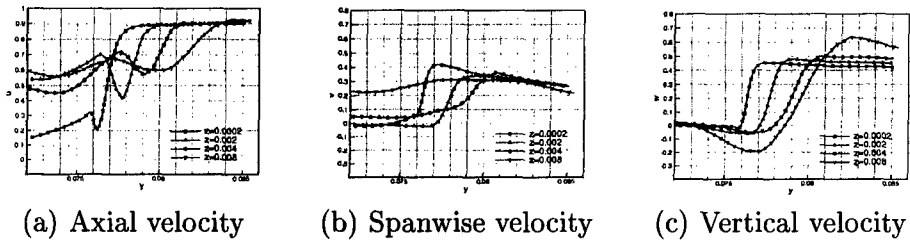

(a) Axial velocity   (b) Spanwise velocity   (c) Vertical velocity

Figure 22. Variations in the three components of time-averaged velocity at the leading-edge with increasing distance from the wing surface within on a cross section at $x = 0.88L$

In Figure 23 the contours of time-averaged pressure on cross sections at $x = 0.31L$, $0.45L$, $0.59L$, $0.73L$, $0.88L$ are displayed. the lowest pressure appears at the center of the primary vortex. The small-scale vortical structures are smeared out by the time-average process. The profiles of time-averaged velocity and pressure along a vertical line passing through the center of the primary vortices are displayed in Figure 24 and 25. The fluid at the center of the primary vortex experiences a acceleration between $x = 0.31L$ and $x = 0.73L$. The pressure decrease along the axial direction within the same region. The large axial velocity excess in the center of the primary vortex is an important feature of the delta wing velocity field. In the experiment, the axial velocity at the center of the primary vortex can reach $1.3U_\infty$, which is smaller than the value predicted by the computation. The vertical position of the vortex center can be identified by the maximum of the velocity profiles. As the size of the primary vortex grows along the axial direction the distance between the vortex center and the wing surface also increases. Near the wing surface, a large slope on the velocity profile is observed at each cross section.

5. Conclusions

Numerical simulation has been carried out to simulate the flow separation around a slender flat-plate delta wing at 12.5° angle of attack. Two Reynolds number have been selected. At a lower Reynolds number of 5×10^4, the flow is stable and dominated by a pair of leading-edge primary vortices. At a higher Reynolds number of 1.96×10^5, the computational results indicate the unsteady instability. The small-scale vortical structures
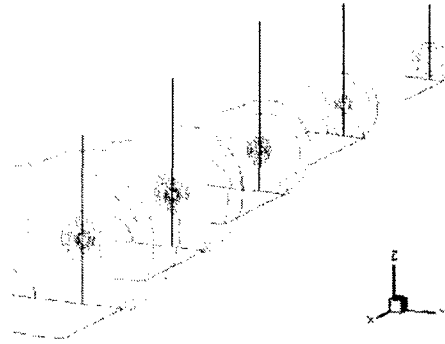
Figure 23.   Contours of time-averaged pressure on selected cross sections.
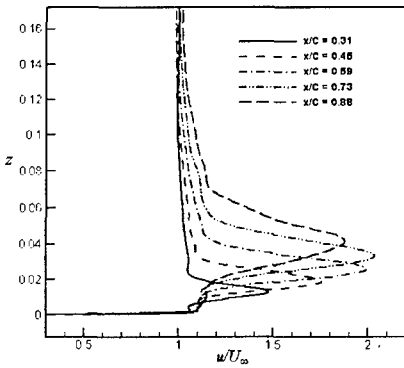

Figure 24.   Profiles of time-averaged axial velocity along a vertical line passing through the center of the primary vortex.
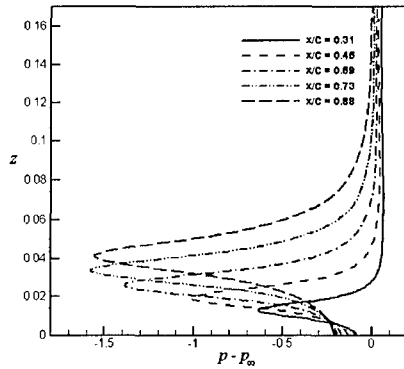
Figure 25.   Profiles of time-averaged pressure along a vertical line passing through the center of the primary vortex.

are shedding from the leading-edge. It has been found that the shedding of the small-scale vortical structures originates not only from the Kelvin-Helmholtz type instability of the leading-edge shear layer, but also from the separation of the secondary vortex form the wing surface, as a result of the interaction between the secondary shear layer and the leading-edge shear layer. The vortex pairing of the small-scale structures are observed. The periods of vortex shedding are obtained from the time series of velocity components. The distributions of the time-averaged velocity near the suction surface of the delta wing obtained from the computational results agree well with those from the experiment of Rieley & Lowson (1998). But the steady small-scale vortical structures which indicate the steady instability observed in the experiment have not been found in the current computational results.

Acknowledgments

References

1. Agrawal, S., Barnett, R. M., and Robinson, B. A. 1992. Numerical investigation of vortex breakdown on a delta wing. *AIAA Journal*, **30**(3), pp.584–591.
2. Cipolla, K. M., Liakopoulos, A., and Rockwell, D. O. 1998. Quantitative imaging in proper orthogonal decomposition of flow past a delta wing. *AIAA Journal*, **36**(7), pp.1247–1255.
3. Cipolla, K. M., and Rockwell, D. 1998. Small-scale vortical structures in crossflow plane of a rolling delta wing. *AIAA Journal*, **36**(12), pp.2276–2278.
4. Delery, J. M. 2001. Robert Legendre And Hener Werle: Toward the Elucidation of Three-dimensional Separation. *Annu. Rev. Fluid Mech.*, **33**, pp.129–154.
5. Gad-el-Hak, M., and Blackwelder, R. F. 1985. The discrete vortices from a delta wing. *AIAA Journal*, **23**(6), pp.961–962.
6. Gordnier, R. E., and Visbal, M. R. 1994. Unsteady vortex structure over delta wing. *Journal of Aircraft*, **31**(1), pp.243–248.
7. Honkan, A., and Andreopoulos, J. 1997. Instantaneous three-dimensional voritcity measurements of vortical flow over a delta wing. *AIAA Journal*, **35**(1), pp.1612–1620.
8. Jiang, L., Shan, H, Liu, C., Visbal, M. R., 1999. Non-reflecting boundary condition in curvilinear coordinates, *Second AFOSR International Conference on DNS/LES*, Rutgers, New Jersey, June 7-9.
9. LeLe, S. K. 1992. Compact finite difference schemes with spectral-like resolution. *J. Comput. Phys.* **103**, pp.16-42.
10. Lowson, M. V. 1988. The three dimensional vortext sheet structure on delta wings. *AGARD CP* 438, Paper 11.
11. Modiano, D. L., and Murman, E. M. 1994. Adative computations of flow around a delta wing with vortex breakdown. *AIAA Journal*, **32**(7), pp.1545–1547.
12. Riley, A. J., and Lowson, M. V. 1998. Development of a three-dimensional free shear layer. *J. Fluid Mech.*, **369**, pp.49–89.
13. Payne, F. M., Ng, T. T., Nelson, R. C., and Shiff, L. B. 1988. Visualization and wake surveys of vortical flow over a delta wing. *AIAA Journal*, **26**(2), pp.137–143.
14. Spekreijse, S.P. (1995) Elliptic grid generation based on Laplace equations and algebraic transformation. *J. Comp. Phys.*, **118**, pp.38–61
15. Visbal, M. R., and Gordnier, R. E. 1995. Origin of computed unsteadiness in the shear layer of a delta wing. *Journal of Aircraft*, **32**(5), pp.1146–1148.
16. Visbal, M. R. 1995. Computational and physical aspects of vortex breaksown on delta wings. *AIAA Paper* 94-2317
17. Visser, K. D., and Nelson, R. C. 1993. Measurements of circulation and vorticity in the leading-edge vortex of a delta wing. *AIAA Journal*, **31**(1), pp.104–111.
18. Winant, C. D, and Browand, F. K. 1974. Vortex pairing: the mechanism of turbulent mixing-layer growth at moderate Reynolds number. *J. Fluid Mech.*, **63**, pp.237–255.
19. Yoon, S., Kwak D. 1992. Implicit Navier-Stokes solver for three-dimensional compressible flows, *AIAA Journal* **30**, pp.2653-2659